Materials Research Bulletin 146 (2022) 111621

Contents lists available at ScienceDirect

Materials Research Bulletin

journal homepage: www.elsevier.com/locate/matresbu

Enhanced photocatalytic activity of $CaMoO_4$/g-C_3N_4 composites obtained via sonochemistry synthesis

Anderson A.G. Santiago [a,*], Elida M. Macedo [a], Fernanda K.F. Oliveira [a], Ricardo L. Tranquilin [b], Marcio D. Teodoro [c], Elson Longo [b], Fabiana V. Motta [a], Mauricio R.D. Bomio [a]

[a] LSQM – Laboratory of Chemical Synthesis of Materials – Department of Materials Engineering, Federal University of Rio Grande do Norte – UFRN, P.O. Box 1524, Natal, RN, Brazil
[b] LIEC, Department of Chemistry, Federal University of São Carlos, 13565-905, São Carlos, SP, Brazil
[c] Department of Physics, Federal University of São Carlos, 13565-905 São Carlos, SP, Brazil

ARTICLE INFO

Keywords:
$CaMoO_4$
g-C_3N_4
sonochemistry
composite
photocatalysis

ABSTRACT

Herein, $CaMoO_4$-based g-C_3N_4 composites are successfully synthesized by the sonochemistry method. All samples present photocatalytic activity under UV-light irradiation by employing methylene blue (MB). The structural analysis is available through X-ray diffraction (XRD), Raman, and FTIR spectroscopies, which verified a scheelite-type tetragonal structure for $CaMoO_4$ with slight distortion in [MoO_4] clusters between samples and confirmation of g-C_3N_4 presence in the powder. FEG-SEM images reveal a higher formation of interfaces between $CaMoO_4$ and g-C_3N_4 particles. Photoluminescence spectra are measured to study the photogenerated charge recombination process. Furthermore, the studies show that increased dosage of g-C_3N_4 onto the composite provides up to 95.1% of MB discoloration in 180 min, while $CaMoO_4$ without g-C_3N_4 only provides 40.2%.

1. Introduction

Composites on a nanometric scale (nanocomposite materials) have shown multiple advances with the enhancement or creation of new properties, which in turn provide an opportunity to develop new applications which were not individually possible for the materials that compose the nanocomposite. Thus, nanocomposite materials can be designed for unique properties, such as improved magnetic, microwave, optical, electrical, and inverse photoconductance performance [1–3].

Studies with materials using graphitic carbon nitride (g-C_3N_4) have attracted much attention for research in the field of composites over the last decade [4–6]. The broad availability of g-C_3N_4 in the earth composed only of carbon and nitrogen and can be prepared by a cheap simple method of heating urea at 500°C [7]. Also, it is a polymeric metal-free semiconductor, has a favorable gap band of ~2.7 eV, high physicochemical stability, interesting electronic structure, and unique optical properties [8,9]. However, bulk g-C_3N_4 shows some disadvantages such as a fast recombination rate of photogenerated electron-hole pairs, small specific surface area, and poor absorption of visible light. Therefore, introducing some functional groups modified with appropriate semiconductors, and coupling with the narrow bandgap semiconductors are some methods to try solving these mentioned problems and increase photocatalytic efficiency [10–12].

Thus, one of the focuses of photocatalysis is wastewater treatment from organic pollutants produced by the textile industries, such as synthetic dyes because they present complex structures and complicated discoloration, resulting in problems to human health and the environment [13]. Photocatalysis is among the most promising of the various alternatives to remove water pollutants, as it constitutes an efficient method and has been gaining considerable prominence in the literature [14,15]. New studies are currently being carried out with materials already consolidated in the literature to reduce the harmful effects on society, such as tungstates and molybdates together with g-C_3N_4, in order to synthesize a composite material showing different or improvement in its properties [16–18]. For example, the $ZnWO_4$/g-C_3N_4 nanocomposite had 98% tetracycline decomposition in 70 min, while $ZnWO_4$ had 21% in the same conditions [19]. In addition, the Bi_2MoO_6/g-C_3N_4 heterojunction presented a 9.2-fold higher capability for ammonia generation than Bi_2MoO_6 in the same conditions [20]. Tetracycline decomposition and capacity for ammonia generation have improved by photogenerated charge carrier partition and heterostructure stabilization [19,20].

* Corresponding author.
E-mail address: andersonsantiago@ufrn.edu.br (A.A.G. Santiago).

https://doi.org/10.1016/j.materresbull.2021.111621
Received 27 July 2021; Received in revised form 4 October 2021; Accepted 26 October 2021
Available online 30 October 2021

Among these materials, calcium molybdate ($CaMoO_4$) may be cited due to being a semiconductor which belongs to the scheelite family, has a tetragonal structure, and a space group I41/a at room temperature [21]. Likewise, its matrices have two clusters, a [CaO_8] deltahedron and a [MoO_4] tetrahedron, with great polarization and stability properties associated with easy distortion of its structure (i.e. decreased symmetries) [22,23]. This material has potential for many industrial applications, such as light-emitting diodes (LEDs) [24,25], sensor and detector [26], and photocatalysis [9]. Furthermore, it has been synthesized by different synthesis methods such as precipitation [27,28], microwave hydro-/solvothermal procedures [9,29], polymeric precursor method [30], spray pyrolysis [22], and sonochemistry [21]. In contrast, the sonochemistry method stands out because it presents uniform particle size, a rapid reaction rate, and high purity at the end of the process [31]. Moreover, the bubble formed during the sonochemistry process can release stored energy through collapse, resulting in a heating and cooling rate of >1010 K/s, a temperature of ~5000 K, and a pressure of ~1000 bar [32]. Thus, the sonochemistry method may be a promising synthesis route for nanocomposite material design, in particular $CaMoO_4$ with g-C_3N_4, in which the $CaMoO_4$ particles will grow on the g-C_3N_4 particles during the synthesis resulting in a strong interaction between particles to improve photogenerated charge carriers and heterostructure stabilization.

In the present work, $CaMoO_4$-based xg-C_3N_4 ($x = 0$, 0.1, 0.2, 0.3, 0.4, and 0.5) composites were successfully synthesized by the sonochemistry method. X-ray diffraction (XRD), Fourier Transform Infrared Spectrophotometer (FTIR), Raman Spectra, FEG-SEM, Photoluminescence, and Ultraviolet-Visible (UV-vis) techniques were utilized to perform structural, morphological and spectroscopy characterizations of the samples. All $CaMoO_4$ based g-C_3N_4 composites performed photocatalysis activity under UV-light irradiation by employing methylene blue (MB). Our finding demonstrates that the $CaMoO_4$/0.5g-C_3N_4 sample is a promising candidate for photocatalysis application with a remarkable value of 95.1% MB discoloration in 180 min.

2. Experiment details

2.1. The synthesis procedure of $CaMoO_4$/g-C_3N_4 composite

Calcium nitrate tetrahydrate [$Ca(NO_3)_2 \cdot 4\ H_2O$] (Synth, 99% purity), sodium molybdenum oxide dihydrate [$MoNa_2O_4 \cdot 2\ H_2O$] (Alfa Aesar, 99.5%), urea [CH_4N_2O] (Synth, 99.0%), nitric acid [HNO_3] (Synth, 65.0%), and distilled water were used as reagents to prepare the $CaMoO_4$/g-C_3N_4 composite. First, graphitic carbon nitride (g-C_3N_4) was prepared by thermal decomposition of 10 g of urea at 550°C in a muffle furnace for 3 hours at a heating rate of 5°C/min [33]. The $CaMoO_4$/g-C_3N_4 precursor solution was then prepared by adding 0.5 mmol of $Ca(NO_3)_2$ and x mmol of g-C_3N_4 in 25 ml of H_2O (forming solution A), and 0.5 mmol of Na_2MoO_4 in 25 ml of H_2O (forming solution B). The values of x were 0, 0.1, 0.2, 0.3, 0.4, and 0.5, where each sample was defined as CMO, CMO1g, CMO2g, CMO3g, CMO4g, and CMO5g, respectively. Solution A was kept in an ultrasonic bath (model 1510 Branson 42 kHz) for 5 min, and solution B was kept under magnetic stirring for 5 min, both at 25°C. Next, solution B was added dropwise in solution A and then HNO_3 was added into this solution to adjust the pH to 7. The solution bottle was then taken to an ultrasonic tip (model Branson 102C, 400W), where it remained for 30 min. After the sonochemistry method, the precipitate formed was washed with water four times and ethanol one time, centrifuged, and dried at 100°C for 12 h.

2.2. Characterization of $CaMoO_4$/g-C_3N_4 composite

Powder XRD patterns of $CaMoO_4$/g-C_3N_4 were collected between the 10° to the 120° angular range with a step speed of 1° min-1 and a step of 0.02° using an XRD 7000 Shimadzu diffractometer and monochromatic Cu Kα radiation. The Rietveld refinement analysis [34] was performed using the General Structure Analysis System (GSAS) with graphic interface EXPGUI [35]. Fourier Transform Infrared Spectrophotometer (FTIR) was used in the range from 400 to 4000 cm^{-1} with a resolution of 8 cm^{-1} (Shimadzu IRTracer-100). The Raman scattering spectra were recorded at room temperature in the frequency range from 100 to 1000 cm^{-1} with a resolution of 2 cm^{-1} and 64 scans using a LabRam HR Evolution HORIBA Scientific with a Nd:YAG laser (633 nm) and the maximum output power was maintained at 100 mW. Field-emission gun scanning electron microscopy and EDS spectroscopy (FESEM; Carl Zeiss, Supra 35-VP Model, Germany, operated at 6 kV or 15 kV) were used to investigate the morphologies and dispersion of atoms of samples. A Shimadzu spectrophotometer (UV-2600 model) was used to determine the UV-visible reflectance spectra of the powders.

Room temperature photoluminescence measurements were carried out using a 355 nm laser (Cobolt/Zouk) as an excitation source focused on a 10 μm spot, with the luminescence dispersed by a 19.3 cm spectrometer with the signal detected by a Si-CCD detector (Andor Kymera/Idus).

The photocatalytic properties of the samples were evaluated for the discoloration of Methylene Blue (MB) dye with a molecular formula [$C_{16}H_{18}ClN_3S$] (99.5% purity, Mallinckrodt) in an aqueous solution under UV-light illumination. The sample was added in a cylindrical quartz reactor, having 50 ml of MB dye solution (concentration 1×10^{-5} mol L^{-1}). Then, a cylindrical quartz reactor was placed into a photoreactor at a controlled temperature (25°C) and illuminated by six UVC lamps (TUV Philips, 15 W, with a maximum intensity of 254 nm = 4.9 eV). A 3 mL aliquot of the dye solution was taken in 30-minute intervals and analyzed for its variations in the maximum absorption band of MB dye solutions by UV–visible absorbance spectra measurements using a Shimadzu spectrophotometer (UV-2600 model).

The mechanism acting on the photocatalytic process was determined using the charge, electron (e^-) and hole (h^+), and hydroxyl radical (•OH) scavengers. Isopropyl alcohol [C_3H_8O] (1 mL alcohol to 100 mL dye), ethylenediaminetetraacetic acid (EDTA) (7.2 mg EDTA/100 mL dye) and, silver nitrate [$AgNO_3$] (8.5 mg $AgNO_3$ to 100 mL dye) were used to suppress the action of hydroxyl radicals (•OH), positive charges (h^+) and negative charges (e^-), respectively.

3. Results and discussion

3.1. X-ray diffraction (XRD)

The XRD patterns of $CaMoO_4$/g-C_3N_4 composites samples are shown in Fig. 1. $CaMoO_4$/g-C_3N_4 composites were indexed in a unit cell with a tetragonal scheelite-type structure with space group *I41/a* (number 88) in accordance with JCPDS 29-0351 and the literature [36–38]. The XRD pattern of the g-C_3N_4 sample used in this work is exhibited in Fig. S1. The sample patterns showed great intensity, meaning they are materials with a long-range crystalline structure. In addition, g-C_3N_4 diffractions were not observed in the composite. Bhosale *et al* [39] synthesized g-C_3N_4/$FeWO_4$ composite and noted that the diffraction referent to the (002) plan of g-C_3N_4 only appeared with clarity when 50/50%wt of each element was prepared. In our work, the mass ratio of $CaMoO_4$/g-C_3N_4 composites had a maximum ratio of 81/19%wt (1:1 in mol, from the precursor reagents), respectively. Thus, the composites only showed the tetragonal phase in the XRD because of the low concentration of g-C_3N_4 regarding $CaMoO_4$.

Fig. S2 and Table 1 show the Rietveld refinement results of XRD patterns. All $CaMoO_4$/g-C_3N_4 XRD patterns were indexed as tetragonal cells (I41/a) according to ICSD 60552 ($CaMoO_4$). The Obs-Calc lines and reliability parameters χ^2, Rp, Rf^2 indicate that the diffraction patterns of the samples are admirably adapted, showing superior quality in the structural refinements and numerical results. The calculated lattice values are according to values found in the literature. Oliveira *et al.* [40] synthesized $CaMoO_4$ by microwave-assisted hydrothermal method, and found lattice values of $a = 5.225$ Å, $c = 11.437$ Å, and cell volume of

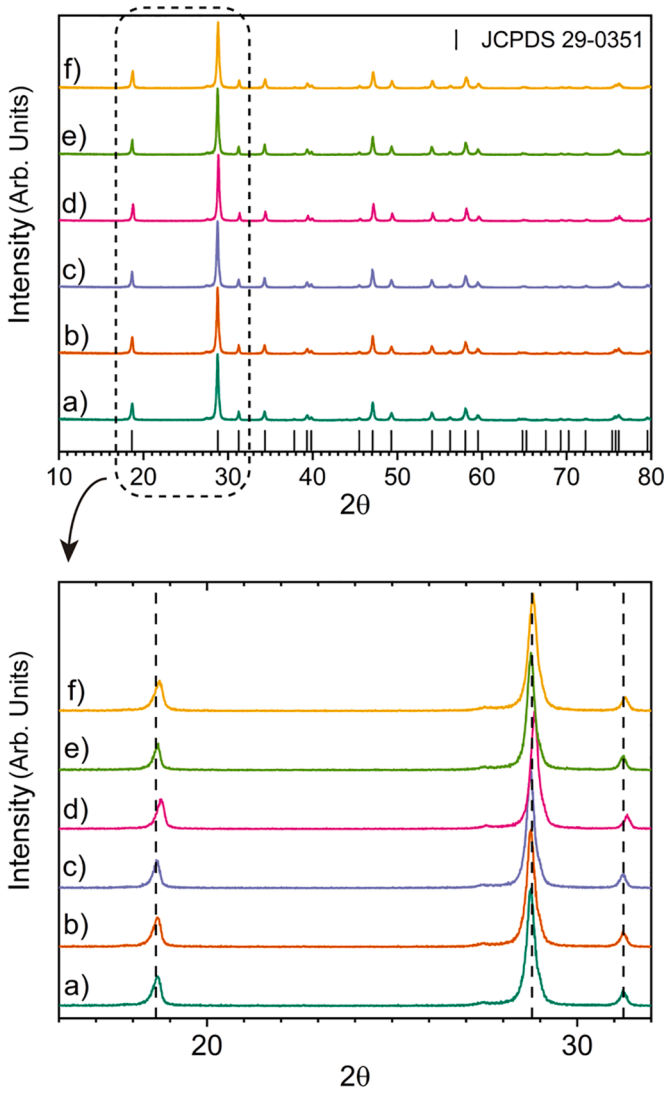

Fig. 1. XRD patterns of $CaMoO_4$/g-C_3N_4, (a) CMO, (b) CMO1g, (c) CMO2g, (d) CMO3g, (e) CMO4g, and (f) CMO5g.

312.25 $Å^3$. The *x, y*, and *z* positions occupied by the Ca and Mo atoms in the unit cell of the $CaMoO_4$ present special positions and are unchanged during structural refinement, where Ca1 cation positions were settled in x = 0.000, y = 0.250, and z = 0.625, and the Mo1 cations were defined at x = 0.000, y = 0.250 and z = 0.125. However, the O1 anions occupy general positions, and x, y, and z positions have been modified, as observable in Table 1. The increase of g-C_3N_4 in the composite caused slight alterations in the lattice, such as decreases of unit cell volume and increases in the *c/a* ratio of the $CaMoO_4$, while crystallite growth occurred non-linearly.

Fig. 2 shows unit cells of $CaMoO_4$/g-C_3N_4 composites modeled using the VESTA program [41]. The $CaMoO_4$ has a tetragonal scheelite-type structure formed by [CaO_8] and [MoO_4] clusters [22], which are highly influenced by the synthesis method conditions. The $CaMoO_4$/g-C_3N_4 composites had slight distortions such as a response to the modification of the synthesis reaction medium with variations of g-C_3N_4 in the composite.

3.2. Fourier Transform Infrared (FTIR) and Raman spectroscopies

The formation of the $CaMoO_4$/g-C_3N_4 composite was confirmed by FTIR and Raman spectroscopies, as can be seen in Fig. 3. In FTIR (Fig. 3-I), the absorption peaks at 765 and 445 cm^{-1} were attributable to the

Table 1
The structural parameters obtained by Rietveld refinement for the $CaMoO_4$/g-C_3N_4 composites.

Sample	CMO	CMO1g	CMO2g	CMO3g	CMO4g	CMO5g
Lattice Parameter						
a (Å)	5.228 (1)	5.229 (9)	5.227 (1)	5.226 (9)	5.226 (1)	5.225 (1)
c (Å)	11.45 (3)	11.45 (3)	11.45 (3)	11.44 (2)	11.45 (3)	11.44 (3)
c/a	2.190 (1)	2.189 (7)	2.190 (5)	2.190 (5)	2.190 (9)	2.189 (4)
Cell Volume ($Å^3$)	312.9 (1)	313.1 (2)	312.8 (1)	312.7 (1)	312.8 (1)	312.6 (1)
Crystallite size (nm)	27(7)	37(3)	29(9)	35(1)	32(5)	25(7)
Microstrain (10^{-3})	0.85 (2)	0.62(1)	0.79(2)	0.66(2)	0.72(1)	0.92(1)
χ^2	1.529	1.620	1.461	1.479	1.436	1.430
Rp (%)	15.39	18.39	14.34	14.24	14.64	13.81
Rf^2 (%)	8.49	13.37	8.49	7.72	8.69	7.71
Atomic position O1						
x	0.146 (8)	0.157 (1)	0.149 (8)	0.147 (7)	0.149 (8)	0.146 (7)
y	0.010 (7)	-0.010 (8)	0.002 (6)	0.010 (6)	-0.003 (7)	0.011 (6)
z	0.210 (3)	0.213 (4)	0.211 (3)	0.210 (3)	0.212 (3)	0.210 (3)

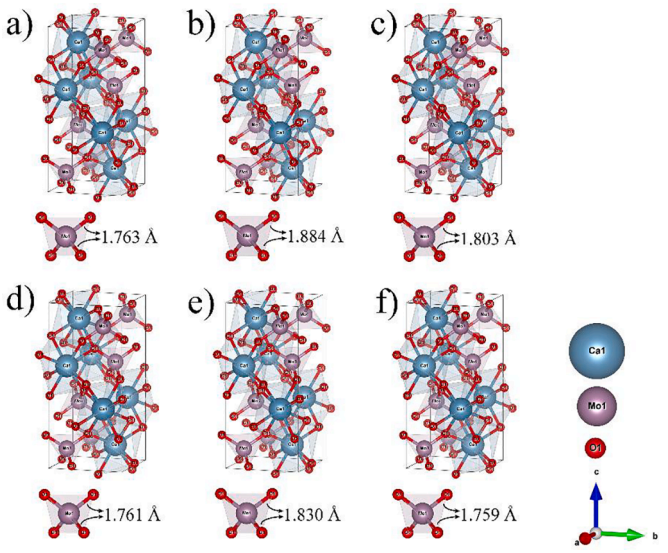

Fig. 2. Tetragonal unit-cell of $CaMoO_4$, namely (a) CMO, (b) CMO1g, (c) CMO2g, (d) CMO3g, (e) CMO4g, and (f) CMO5g.

asymmetric stretching vibration of O-Mo-O vibration in the MoO_4^{2-} tetrahedron and to the bending of Mo-O vibration of the Au mode, respectively [42,43]. The absorption peak at 1638 cm^{-1} was assigned to the C=N stretching vibration mode, while the bands at 1241, 1325, 1407, 1465, and 1568 cm^{-1} were ascribed to aromatic C-N stretching vibration modes [44,45]. These absorption peaks increase with the increase of g-C_3N_4 on the composite. The wideband at 3419 cm^{-1} is attributed to -OH from water or ethanol [46]. In contrast, a band at 2920 cm^{-1} is attributed to the C-H stretching vibration from ethanol [46].

Raman spectroscopy (Fig. 3-II) was utilized to confirm the vibrational properties of $CaMoO_4$/g-C_3N_4 composites. The materials with scheelite structure have internal vibration referent to the oscillations inside the [MoO_4] molecular group, and external vibration referent to the motion of the cation and the rigid molecular unit [47,48]. $CaMoO_4$ crystals showed 26 different vibrations according to group theory calculations, as characterized by:

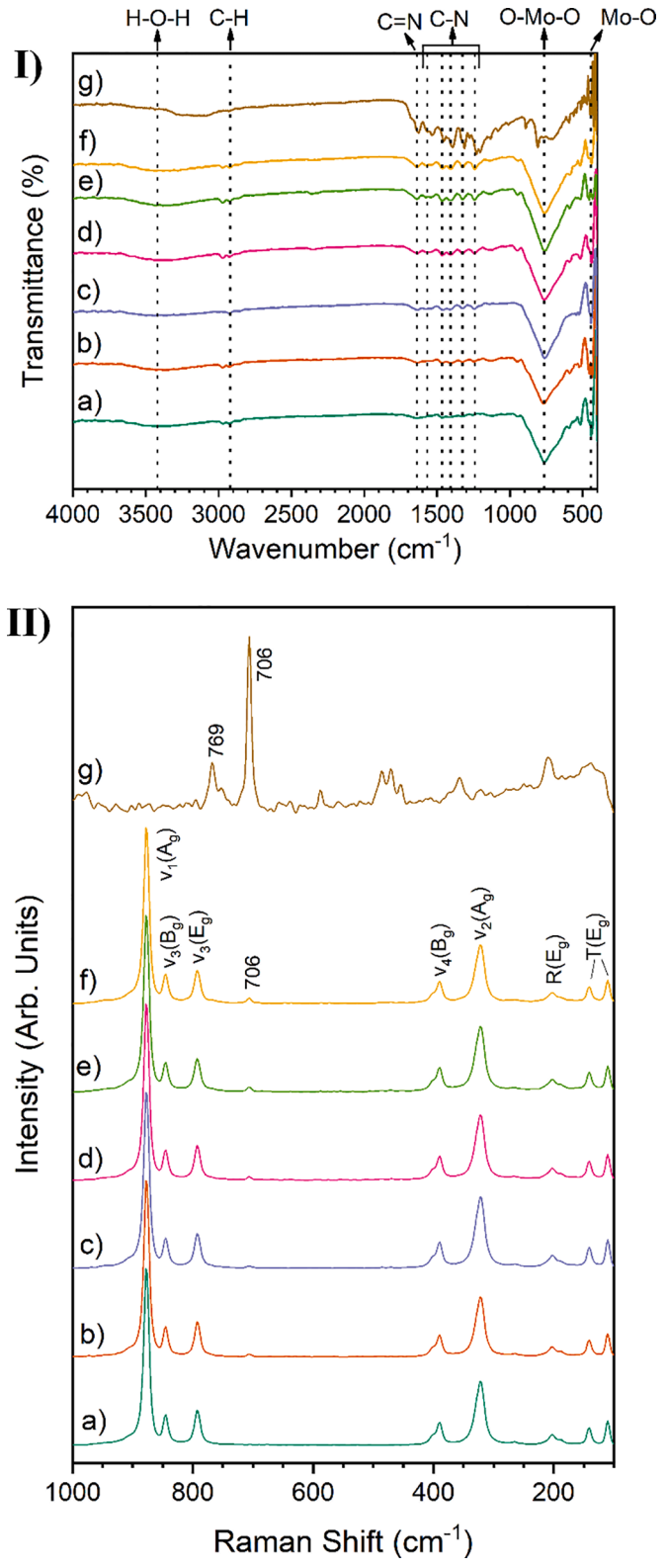

Fig. 3. FTIR (I) and Raman (II) of $CaMoO_4$/g-C_3N_4 being (a) CMO, (b) CMO1g, (c) CMO2g, (d) CMO3g, (e) CMO4g, (f) CMO5g, and (g) g-C_3N_4 pure.

$$\Gamma = 3A_g + 5A_u + 5B_g + 3B_u + 5E_g + 5E_u \quad (1)$$

where the A_g, B_g, and E_g are Raman-active vibration modes and the A and B modes are non-degenerating, while the E modes are doubly degenerating. In addition, the subscripts (g) and (u) represent the parity under inversion in centrosymmetric $CaMoO_4$ crystals. Thus, the A_u and E_u modes correspond to the zero frequency of acoustic modes, but the others are optic modes. Moreover, the A_g, B_g, and E_g modes occur from the same motion of the $CaMoO_4$ crystal [38,49]. Consequently, $CaMoO_4$ crystals are estimated by 13 zone-center Raman-active modes, as represented by:

$$\Gamma_{Raman} = 3A_g + 5B_g + 5E_g \quad (2)$$

Also, Raman spectra of molybdates can be classified into two groups: external, which corresponds to the lattice phonon, which corresponds to the motion of [CaO_8] clusters and the rigid cell units; and internal, which relates to the vibration inside [MoO_4] cluster units, considering the center of mass in the stationary state [38,49].

Several peaks were observed in Fig. 3-II(a-f) referent to the Raman-active internal modes of tetrahedral MoO_4: $\nu_1(A_g)$, $\nu_3(B_g)$, $\nu_3(Eg)$, $\nu_4(B_g)$, $\nu_2(A_g)$, R(E_g), and external T (E_gE_g). Ten modes of the $CaMoO_4$ crystal were identified and their frequencies presented values close to the values found for the theoretical frequency values [38], as can be seen in Table S1. The Raman spectrum of g-C_3N_4 is characteristic of several peaks due to the surface defects and disorders located at the edges of the graphite platelets [50]. Moreover, the band in 706 cm^{-1} is assimilated to the breathing modes of the triazine ring [51]. The peak in 769 cm^{-1} is assigned to the out-of-plane bending modes of graphitic domains [51], as seen in Fig. 3-II(g). The presence of 706 cm^{-1} peaks referent to g-C_3N_4 is observed in $CaMoO_4$/g-C_3N_4 composites validating the occupancy of g-C_3N_4 jointly with $CaMoO_4$.

3.3. Morphological characterization

Fig. 4 shows the micrographs of the CaMoO4/g-C_3N_4 composites. The CMO particles formed by several nanoparticles form a cauliflower-like shape (Fig. 4a), while g-C_3N_4 particles presented a nanosheet-like structure (Fig. 4g). The $CaMoO_4$ morphology is very dependent on the pH of the precursor solution and the sonochemistry synthesis time. Zhang *et al.* [52] and Wang *et al.* [53] demonstrated that CaMoO4 particles obtained by sonochemistry have their morphology changed according to solution pH, time, and the Ca/Mo ratio, with morphology varying between flower-, elliptical-, cauliflower- and spindle-shapes, for example. Thus, our samples have similar morphology because they were synthesized under equal pH, time, and Ca/Mo ratio conditions. However, the addition of g-C_3N_4 promoted nucleation points on its surface for the growth of $CaMoO_4$ particles, in which g-C_3N_4 particles were observed among several $CaMoO_4$ particles, as can be seen by EDS mapping in Fig. S3. This phenomenon occurs because the energy required for heterogeneous nucleation is less than the energy needed for nucleation in free space [54]. Also, the increase in g-C_3N_4 in the composite can favor observation of this phenomenon, raise interface formation between $CaMoO_4$ and g-C_3N_4 particles, and improve the composite properties.

3.4. Optical properties

Fig. 5 depicts the absorbance spectra (5A), estimated values (5B), and photoluminescence spectra (5C) for the bandgap energy of $CaMoO_4$/g-C_3N_4 composites. Bandgap energy (E_{gap}) values were estimated using the Kubelka-Munk function [55], followed by the Wood and Tauc method [56] because this analysis has been successfully used in many ternary oxides related to $CaMoO_4$ [57]. Bandgap energy (E_{gap}) values were estimated by $\alpha h\nu \propto (h\nu\text{-}E_{gap})^{1/p}$ [56], where α is the absorbance, h is the Planck constant, ν is the frequency, and p indicates the different kinds of transitions. Molybdates with a scheelite-type tetragonal structure have been reported with a permitted direct electronic transition [58,59], so the results from $CaMoO_4$/g-C_3N_4 composites were analyzed assuming $p = 1/2$. The bandgap energy values of the CMO and g-C_3N_4 samples (Fig. 5B) are in accordance with the literature [60–63]. The remaining samples showed a bandgap value between CMO and

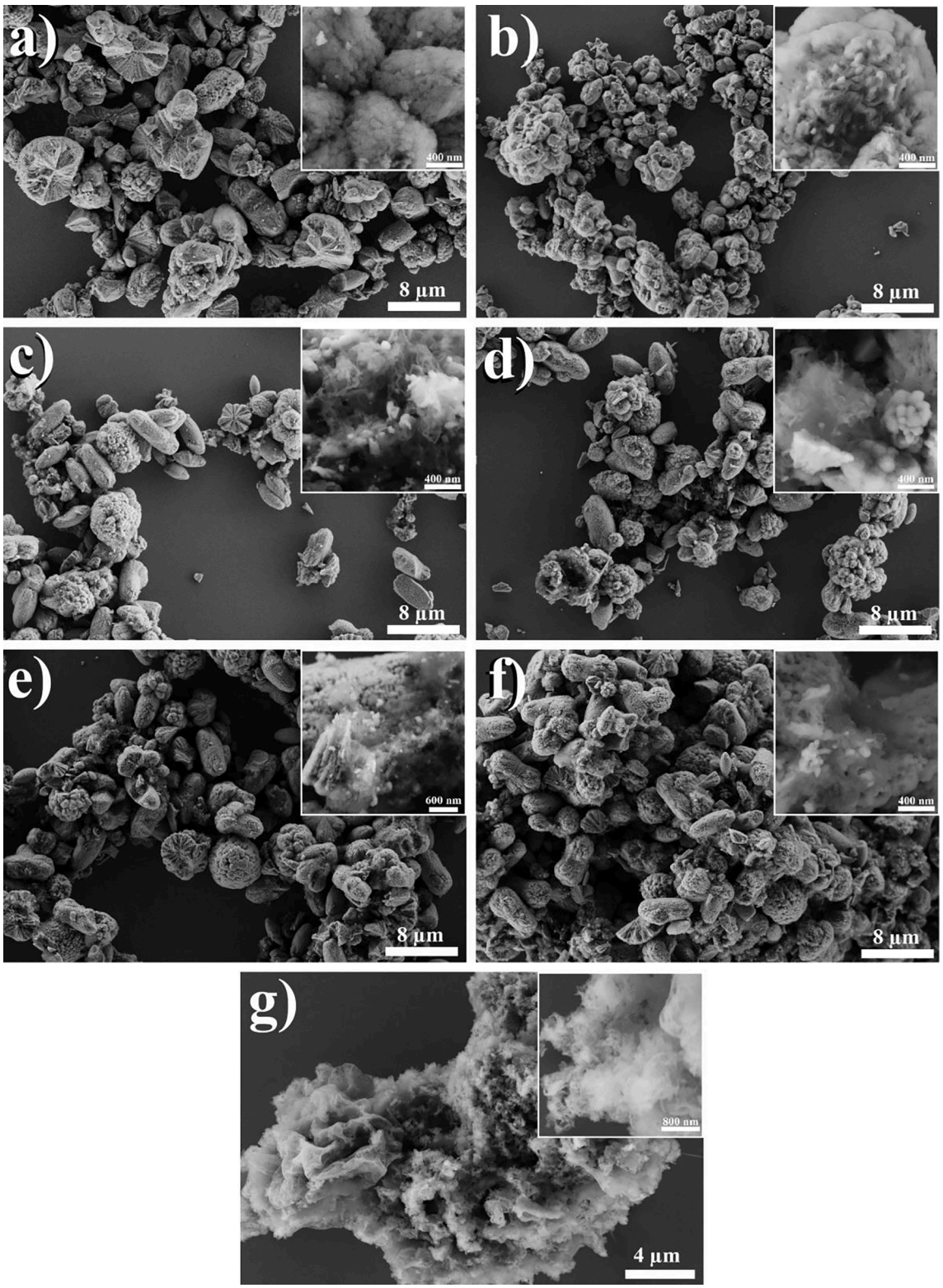

Fig. 4. FESEM images of $CaMoO_4/g\text{-}C_3N_4$, namely (a) CMO, (b) CMO1g, (c) CMO2g, (d) CMO3g, (e) CMO4g, (f) CMO5g, and (g) $g\text{-}C_3N_4$ pure.

$g\text{-}C_3N_4$ samples. Additionally, an increase of $g\text{-}C_3N_4$ in the composite resulted in a bandgap value reduction and may provide conversion efficiency improvement of light irradiated in the photocatalytic process of $CaMoO_4/g\text{-}C_3N_4$ composites regarding pure $CaMoO_4$.

Photoluminescence spectra were measured to study the photogenerated charge recombination process of the $CaMoO_4/g\text{-}C_3N_4$ samples, as can be seen in Fig. 5C. The $g\text{-}C_3N_4$ sample showed the highest PL intensity with a peak centered around 475 nm, and the $CaMoO_4$ sample exhibited the lowest PL intensity with broadband centered around 525 nm. The strong PL signal of $g\text{-}C_3N_4$ is related to the quick recombination of photoexcited carriers, which can lead to poor performance in photocatalytic processes [64,65]. However, the PL intensity of the $CaMoO_4/g\text{-}C_3N_4$ composite had a significant decrease with the CMO5g sample (lowest intensity), which results from a low recombination rate

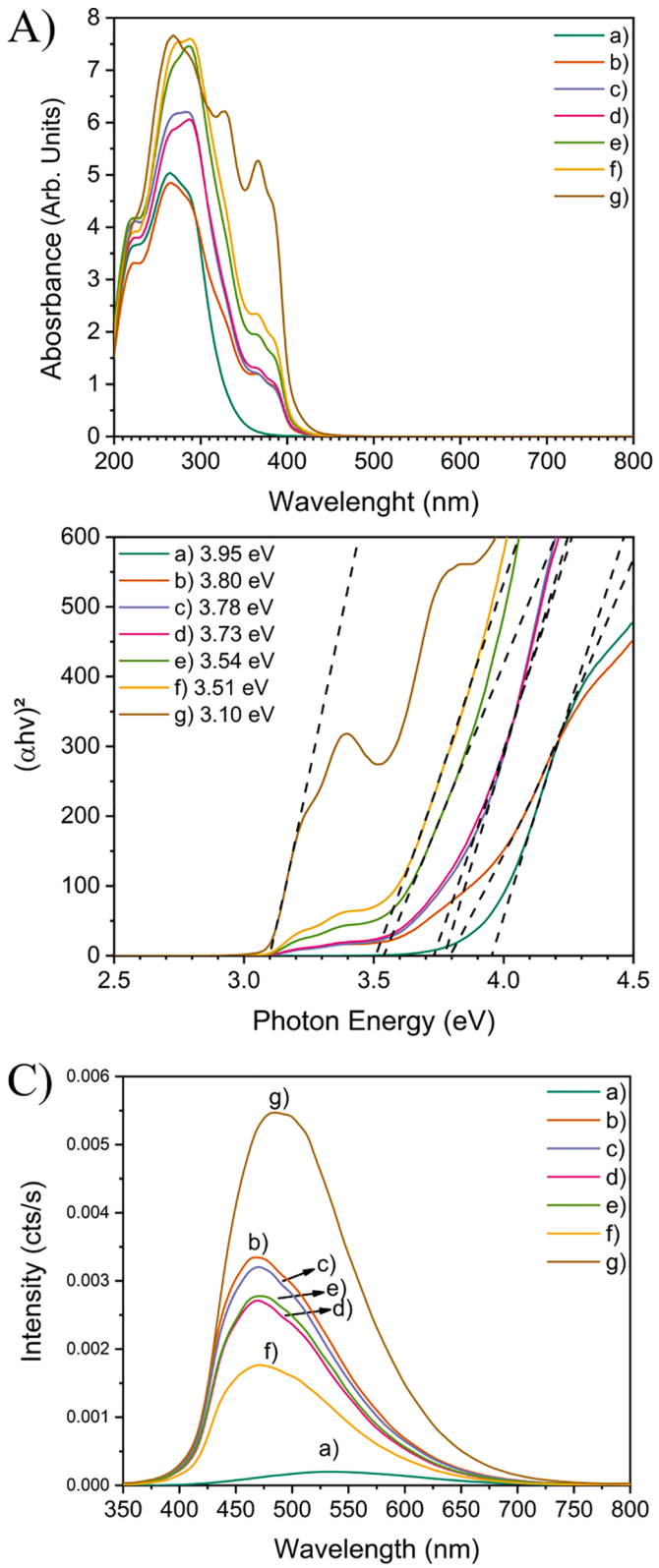

Fig. 5. (A) Absorbance spectra, (B) the bandgap values, and (C) Photoluminescence spectra of $CaMoO_4$/g-C_3N_4, namely (a) CMO, (b) CMO1g, (c) CMO2g, (d) CMO3g, (e) CMO4g, (f) CMO5g, and (g) pure g-C_3N_4.

of the photoexcited carriers. Thus, PL spectra may suggest a strong interaction and photogenerated carrier transfer between g-C_3N_4 and $CaMoO_4$.

3.5. Photocatalytic Activity

The photocatalytic activity of the $CaMoO_4$/g-C_3N_4 composites was examined with methylene blue (MB) under UV-Vis radiation ($\lambda \geq 254$ nm) for 180 minutes. As shown in Fig. 6a, the CMO sample shows low efficiency to MB discoloration in 180 minutes. On the other hand, discoloration efficiency increases when g-C_3N_4 was added to CMO. The CMO5g sample showed 95.1% of MB discoloration in 180 min, while the CMO sample had only 40.2%. Furthermore, the dye adsorption process on the photocatalyst particles increased with the insertion of g-C_3N_4, as observable in Fig. 6a. This phenomenon may be related to the greater surface area observed in nanosheet-like particles of g-C_3N_4, resulting in higher dye-particle interaction. However, the literature presents that $CaMoO_4$ generally has a low surface area, around 1 to 9 m^2/g [66–68], while g-C_3N_4 obtained at 550°C have surface area of 64.3 m^2/g [33]. Moreover, the composite formation improved photocatalytic activity performance and confirmed photogenerated carrier transfer between g-C_3N_4 and $CaMoO_4$, as observable in the photoluminescence results (Fig. 5C). The photocatalytic process can be described by the pseudo-first-order kinetic model (Equation 3) [69] as shown in Fig. 6b.

$$\ln(C_t / C) = k_i \, . \, t \tag{3}$$

In which: *ki* is the kinetic rate constant; *C* is the original concentration of MB dye; *Ct* is the MB dye concentration at time *t*. It is observable that the kinetic constant *k* increases as g-C_3N_4 increases, showing that the g-C_3N_4 concentration increase in the composite promotes higher MB dye discoloration.

The capacity to produce e^-/h^+ radicals is decisive in the performance of photocatalysts due to these radicals reacting with oxygen to produce oxidizing species such as superoxide radical anion ($\bullet O_2^-$) and

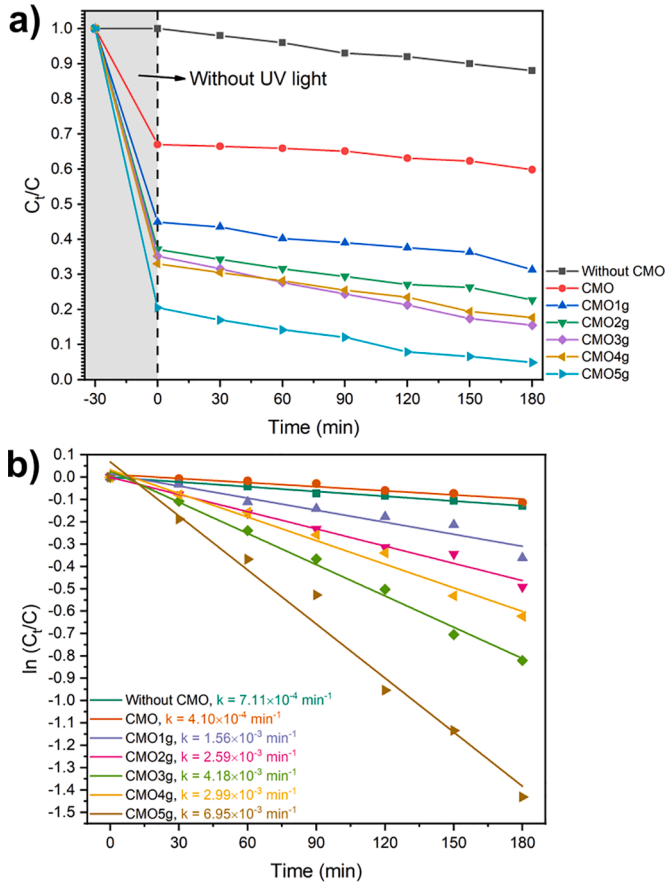

Fig. 6. Variation of the MB dye discoloration as a function of the time (a) and kinetic discoloration evolution of (b) $CaMoO_4$/g-C_3N_4 composites.

hydroxyl radicals (•OH) which are dependent on conduction band (CB) and valence band (VB) potentials. These potentials are calculated using the following empirical equations [70]:

$$E_{CB} = \chi - E_e - 0.5E_{gap} \quad (4)$$

$$E_{VB} = E_{CB} + E_{gap} \quad (5)$$

In which: E_{VB} and E_{CB} are the valence (VB) and conduction (CB) potentials, respectively, E_e is the energy of free electrons vs. hydrogen (4.5 eV), E_{gap} is the bandgap energy of the semiconductor, and χ is the electronegativity of semiconductor. In turn, χ was calculated by the following equation [71]:

$$\chi = \left[x(A)^a x(B)^b x(C)^c\right]^{1/(a+b+c)} \quad (6)$$

In which: a, b, and c are the number of atoms in the compounds. The χ value for $CaMoO_4$ is 5.82 eV, and equivalent ECB and E_{VB} values are -0.65 eV/NHE and +3.30 eV/NHE, respectively. However, the χ value for g-C_3N_4 is 4.72 eV [72], and the equivalent E_{CB} and E_{VB} values are -1.33 eV/NHE and +1.77 eV/NHE, respectively. The UV radiation used may have allowed the excitation and generation of electron-hole pairs in both $CaMoO_4$ and g-C_3N_4, as observable in Fig. 7a. However, the ECB of g-C_3N_4 is less than the E_{CB} of $CaMoO_4$ and may result in an easily-photoinduced electron transfer from CB of g-C_3N_4 to CB $CaMoO_4$. Thus, the electrons in the CB $CaMoO_4$ are trapped by O_2 to form $\bullet O_2^-$, because the E_{CB} value of $CaMoO_4$ is smaller than the $E(O_2/\bullet O_2^-)$ (-0.33 eV/NHE [73]). On the other hand, the holes formed in the VB of $CaMoO_4$ can easily migrate to VB of g-C_3N_4 because the E_{VB} value of $CaMoO_4$ is larger than the E_{VB} of g-C_3N_4. However, the holes localized in the VB g-C_3N_4 cannot react with OH^- or H_2O to form •OH, as the $E(\bullet OH/H_2O)$ value (+2.38 eV/NHE [73]) is superior to E_{VB} of g-C_3N_4. Also, the interaction of OH^- or H_2O with holes localized in the VB $CaMoO_4$ can result in the formation of •OH because the $E(\bullet OH/H_2O)$ value is less than the E_{VB} $CaMoO_4$ value.

The EDTA, isopropyl alcohol, and $AgNO_3$ were utilized as inhibitors of h^+, •OH, and e^-, respectively [13]. The inhibitors were used to verify the photocatalytic mechanism of the $CaMoO_4$/g-C_3N_4 composite. As shown in Fig. 7b-c, the addition of EDTA and isopropyl alcohol reduced the photocatalytic activity, while the use of silver nitrate increased the discoloration capacity of CMO and CMO5g samples. Then, the principal mechanism acting on the photocatalytic activity is of the O_2^- because EDTA suppresses the h^+ and raises the number of electrons during the photocatalytic process. Next, dye oxidation is a secondary acting mechanism because isopropyl alcohol suppresses the •OH radicals and reduces the oxidative capacity of the photocatalyst. According to the results, the photocatalytic process of MB discoloration over $CaMoO_4$/g-C_3N_4 composite is described as:

$$gC_3N_4 + hv \rightarrow gC_3N_4(e^-) + gC_3N_4(h^+) \quad (7)$$

$$CaMoO_4 + hv \rightarrow CaMoO_4(e^-) + CaMoO_4(h^+) \quad (8)$$

$$gC_3N_4(e^-) \rightarrow CaMoO_4(e^-) \quad (9)$$

$$CaMoO_4(e^-) + O_2 \rightarrow \cdot O_2^- \quad (10)$$

$$CaMoO_4(h^+) + OH^- \rightarrow CaMoO_4 + \cdot OH \quad (11)$$

$$\cdot O_2^-, h^+, \cdot OH + MB \rightarrow CO_2 + H_2O + \text{other inorganic molecules} \quad (12)$$

Fig. 8 shows the cyclic stability test of the CMO5g sample. As can be seen, there is little alteration in the photocatalytic capacity of the sample between the four consecutive cycles, in which the 1st, 2nd, 3rd and 4th cycles had 95%, 100%, 99% and 97% of MB discoloration, respectively. This result indicates that even with the application of consecutive cycles, the loss in photocatalytic efficiency is small and allows this composite to be applied in consecutive cycles.

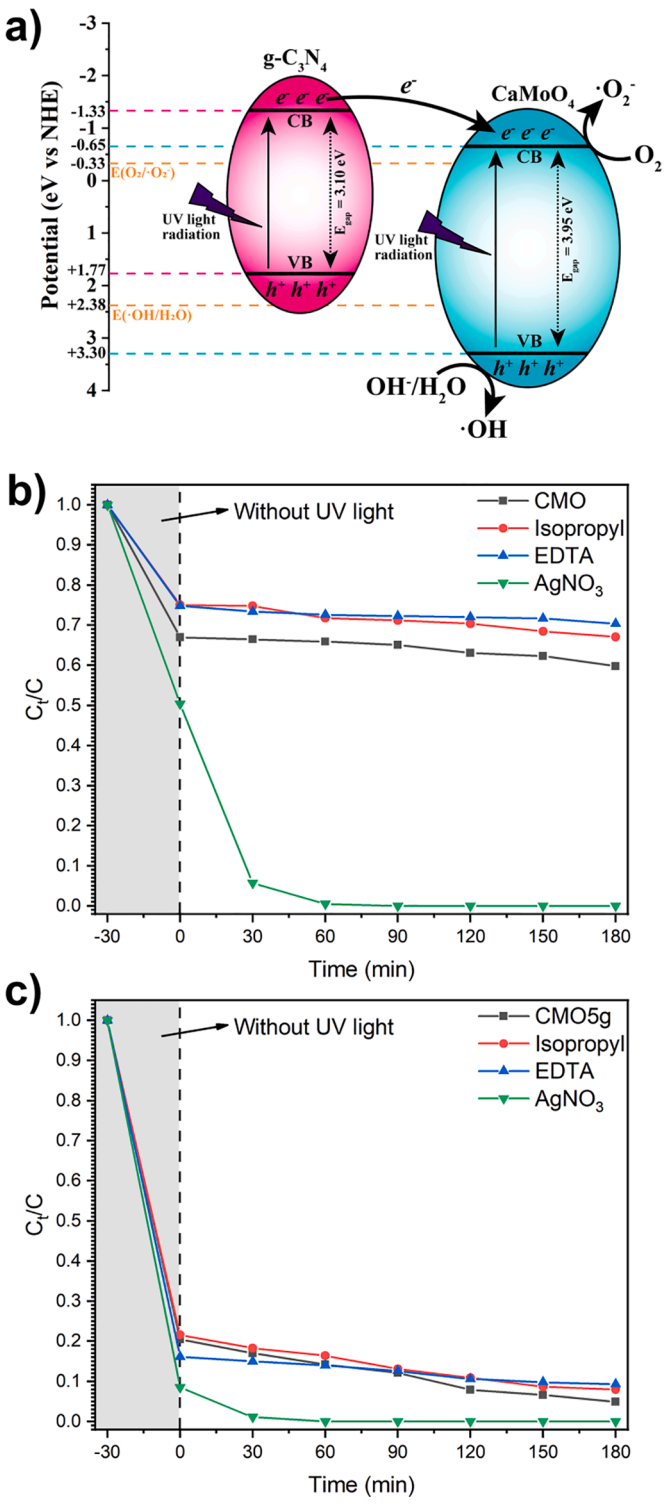

Fig. 7. (a) Schematic illustration of the charge transfer pathway of the $CaMoO_4$/g-C_3N_4 composite catalyst under UV light irradiation and variation of the MB dye concentration for the (b) CMO and (c) CMO5g samples with and without charge inhibitors.

4. Conclusion

$CaMoO_4$-based g-C_3N_4 composites were successfully synthesized by the sonochemistry method with 0, 0.1, 0.2, 0.3, 0.4, and 0.5 of g-C_3N_4. The powders were characterized by X-ray diffraction (XRD), FT-IR, and Raman spectroscopies revealing crystals with a tetragonal scheelite

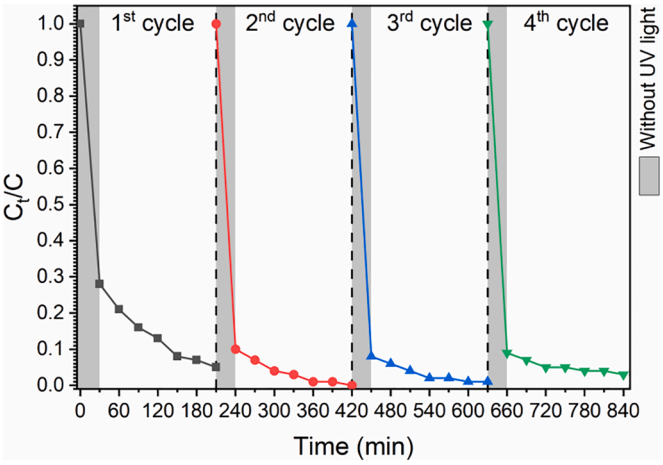

Fig. 8. Photocatalytic curves from cyclic stability test of CMO5g sample.

structure and long-range order and confirmed the presence of g-C_3N_4 in the samples. FEG-SEM micrographs of nanoparticles $CaMoO_4$ exhibited a cauliflower-like shape, while g-C_3N_4 particles presented a nanosheet-like morphology.

Photoluminescence spectra were also measured to study the photogenerated charge recombination process. In addition, the photocatalysis results showed that the g-C_3N_4 insertion into the composite favored the photocatalytic activity performance, in which there was an increase in photocatalytic activity from 40.2% (CMO) to 95.1% (CMO5g) due to photogenerated carrier transfer between g-C_3N_4 and $CaMoO_4$. This phenomenon occurs by easy photoinduced electron transfer from CB of g-C_3N_4 to CB $CaMoO_4$ and easy migration of holes formed in the VB of $CaMoO_4$ to VB of g-C_3N_4. Also, the trapping experiment showed that principal mechanism acting on the photocatalytic activity is O_2^-. Thus, a $CaMoO_4$/0.5g-C_3N_4 composite obtained by the sonochemistry method is a promising photocatalyst candidate since a value of 95.1% of MB discoloration in 180 min was observed with maintenance of its photocatalytic properties after consecutive use cycles. Finally, this study presents a new vision for the synthesis of nanocomposite materials with g-C_3N_4 by the sonochemistry method, enabling the synthesis of different binary oxides or ternary oxides, whether doped or undoped, together with g-C_3N_4 in different proportions in a simple way for improving properties.

CRediT authorship contribution statement

Anderson A.G. Santiago: Methodology, Visualization, Writing – original draft. **Elida M. Macedo:** Investigation, Methodology. **Fernanda K.F. Oliveira:** Writing – original draft. **Ricardo L. Tranquilin:** Investigation, Data curation. **Marcio D. Teodoro:** Data curation, Resources. **Elson Longo:** Resources. **Fabiana V. Motta:** Supervision. **Mauricio R.D. Bomio:** Writing – review & editing, Project administration.

Declaration of Competing Interest

The authors declare no competing financial interest.

Acknowledgment

The authors thank the following Brazilian research financing institutions for financial support: A.A.G. Santiago and M.R.D. Bomio acknowledges the financial support from the National Council for Scientific and Technological Development (*CNPq*) – Finance codes (140231/2018-8) and (303657/2017-0), respectively; the Coordination for the Improvement of Higher Education Personnel (CAPES) – Brazil with Finance Code 001; the Graduate Program in Materials Science and Engineering (PPGCEM-UFRN); and the Sao Paulo Research Foundation (*FAPESP*) (Process 2013/07296-2).

Supplementary materials

Supplementary material associated with this article can be found, in the online version, at doi:10.1016/j.materresbull.2021.111621.

References

[1] S. Rahman, S. Samanta, A. Kuzmin, D. Errandonea, H. Saqib, D.L. Brewe, J. Kim, J. Lu, L. Wang, Tuning the Photoresponse of Nano-Heterojunction: Pressure-Induced Inverse Photoconductance in Functionalized WO_3 Nanocuboids, Advanced Science 6 (2019), 1901132.
[2] R. Peymanfar, F. Fazlalizadeh, Fabrication of expanded carbon microspheres/$ZnAl_2O_4$ nanocomposite and investigation of its microwave, magnetic, and optical performance, J. Alloys Compd. 854 (2021), 157273.
[3] A.M.A. Henaish, B.I. Salem, T.M. Meaz, Y.A. Alibwaini, A.-W. Ajlouni, O. M. Hemeda, E.A. Arrasheed, Synthesize, characterization, dielectric, linear and nonlinear optical properties of Ni–Al Ferrite/PANI nanocomposite film, Opt. Mater. 119 (2021), 111397.
[4] S.C. Yan, Z.S. Li, Z.G. Zou, Photodegradation of rhodamine B and methyl orange over boron-doped g-C_3N_4 under visible light irradiation, Langmuir 26 (2010) 3894–3901.
[5] Y. He, L. Zhang, B. Teng, M. Fan, New application of Z-scheme Ag_3PO_4/g-C_3N_4 composite in converting CO_2 to fuel, Environ Sci Technol 49 (2015) 649–656.
[6] J. Liao, W. Cui, J. Li, J. Sheng, H. Wang, P. Chen, G. Jiang, Z. Wang, F. Dong, Nitrogen defect structure and NO^+ intermediate promoted photocatalytic NO removal on H_2 treated g-C_3N_4, Chem. Eng. J. 379 (2020), 122282.
[7] W. Hu, J. Yu, X. Jiang, X. Liu, R. Jin, Y. Lu, L. Zhao, Y. Wu, Y. He, Enhanced photocatalytic activity of g-C_3N_4 via modification of $NiMoO_4$ nanorods, Colloids Surf. A Physicochem. Eng. Asp. 514 (2017) 98–106.
[8] T. Xiong, W. Cen, Y. Zhang, F. Dong, Bridging the g-C_3N_4 interlayers for enhanced photocatalysis, ACS Catal 6 (2016) 2462–2472.
[9] E. Pavitra, G.S.R. Raju, S.M. Ghoreishian, L.K. Bharat, S.R. Dugasani, J.Y. Park, S. H. Park, J.S. Yu, Y.-K. Han, Y.S. Huh, Streptavidin activated hydroxyl radicals enhanced photocatalytic and photoelectrochemical properties of membrane-bound like $CaMoO_4$:Eu^{3+} hybrid structures, J. Mater. Chem. A 7 (2019) 23105–23120.
[10] E. Vesali-Kermani, A. Habibi-Yangjeh, H. Diarmand-Khalilabad, S. Ghosh, Nitrogen photofixation ability of g-C_3N_4 nanosheets/Bi_2MoO_6 heterojunction photocatalyst under visible-light illumination, J Colloid Interface Sci 563 (2020) 81–91.
[11] F. Mei, K. Dai, J. Zhang, W. Li, C. Liang, Construction of Ag SPR-promoted step-scheme porous g-C_3N_4/Ag_3VO_4 heterojunction for improving photocatalytic activity, Appl. Surf. Sci. 488 (2019) 151–160.
[12] S. Zhao, J. Wu, Y. Xu, Z. Wang, Y. Han, X. Zhang, Ag_2CO_3-derived Ag/g-C_3N_4 composite with enhanced visible-light photocatalytic activity for hydrogen production from water splitting, Int. J. Hydrog. Energy (2020).
[13] A.A.G. Santiago, E.M. Macedo, F.K.F. Oliveira, F.V. Motta, M.R.D. Bomio, Synthesis and characterization of $BaWO_4$:xTm^{3+},yPr^{3+} obtained by ultrasonic spray pyrolysis, J. Mater. Sci. Mater. Electron. 31 (2020) 11599–11608.
[14] A.A.G. Santiago, N.F. Andrade Neto, E. Longo, C.A. Paskocimas, F.V. Motta, M.R. D. Bomio, Fast and continuous obtaining of Eu^{3+} doped CeO_2 microspheres by ultrasonic spray pyrolysis: characterization and photocatalytic activity, J. Mater. Sci. Mater. Electron. 30 (2019) 11508–11519.
[15] E.A.C. Ferreira, N.F.A. Neto, A.A.G. Santiago, C.A. Paskocimas, M.R.D. Bomio, F. V. Motta, Synthesis and characterization of α-Ag_2MoO_4/β-Ag_2MoO_4 heterostructure obtained by fast and simple ultrasonic spray pyrolysis method at different temperatures, J. Mater. Sci. Mater. Electron. 31 (2020) 4271–4278.
[16] Y. Huo, Z. Wang, J. Zhang, C. Liang, K. Dai, Ag SPR-promoted 2D porous g-C_3N_4/Ag_2MoO_4 composites for enhanced photocatalytic performance towards methylene blue degradation, Appl. Surf. Sci. 459 (2018) 271–280.
[17] M. Sumathi, A. Prakasam, P. Anbarasan, A facile microwave stimulated g-C_3N_4/α-Fe_2O_3 hybrid photocatalyst with superior photocatalytic activity and attractive cycling stability, J. Mater. Sci. Mater. Electron. 30 (2019) 10985–10993.
[18] H. Li, J. Liu, W. Hou, N. Du, R. Zhang, X. Tao, Synthesis and characterization of g-C_3N_4/Bi_2MoO_6 heterojunctions with enhanced visible light photocatalytic activity, Appl. Catal. B 160-161 (2014) 89–97.
[19] C.V. Reddy, R. Koutavarapu, I.N. Reddy, J. Shim, Effect of a novel one-dimensional zinc tungsten oxide nanorods anchored two-dimensional graphitic carbon nitride nanosheets for improved solar-light-driven photocatalytic removal of toxic pollutants and photoelectrochemical water splitting, J. Mater. Sci. Mater. Electron. 32 (2021) 33–46.
[20] E. Vesali-Kermani, A. Habibi-Yangjeh, H. Diarmand-Khalilabad, S. Ghosh, Nitrogen photofixation ability of g-C_3N_4 nanosheets/Bi_2MoO_6 heterojunction photocatalyst under visible-light illumination, J. Colloid Interface Sci. 563 (2020) 81–91.
[21] S.S. Hosseinpour-Mashkani, S.S. Hosseinpour-Mashkani, A. Sobhani-Nasab, Synthesis and characterization of rod-like $CaMoO_4$ nanostructure via free surfactant sonochemical route and its photocatalytic application, J. Mater. Sci. Mater. Electron. 27 (2016) 4351–4355.
[22] C.R.R. Almeida, L.X. Lovisa, A.A.G. Santiago, M.S. Li, E. Longo, C.A. Paskocimas, F. V. Motta, M.R.D. Bomio, One-step synthesis of $CaMoO_4$:Eu^{3+} nanospheres by ultrasonic spray pyrolysis, J. Mater. Sci. Mater. Electron. 28 (2017) 16867–16879.

[23] S. Sinha, M.K. Mahata, K. Kumar, S.P. Tiwari, V.K. Rai, Dualistic temperature sensing in Er^{3+}/Yb^{3+} doped $CaMoO_4$ upconversion phosphor, Spectrochim. Acta A 173 (2017) 369–375.

[24] A.I. Becerro, M. Allix, M. Laguna, D. González-Mancebo, C. Genevois, A. Caballero, G. Lozano, N.O. Núñez, M. Ocaña, Revealing the substitution mechanism in Eu^{3+}:$CaMoO_4$ and Eu^{3+}, Na^+:$CaMoO_4$ phosphors, J. Mater. Chem. C 6 (2018) 12830–12840.

[25] L. Jinping, T. ZHANG, Z. Gangqiang, Z. Hairong, Up-conversion photoluminescence emissions of $CaMoO_4$:Pr^{3+}/Yb^{3+} powder, J. Rare Earths 35 (2017) 645–651.

[26] R. Dey, V.K. Rai, Er^{3+}-Tm^{3+}-Yb^{3+}:$CaMoO_4$ phosphor as an outstanding upconversion-based optical temperature sensor and optical heater, Methods Appl. Fluoresc. 5 (2017), 015006.

[27] S. Karki, P. Aryal, D. Ha, H.J. Kim, H.K. Park, I.R. Pandey, Synthesis, Luminescence and Optical Properties of a $CaMoO_4$ Nano-Powder Prepared by Using the Precipitation Method, J Korean Phys Soc 75 (2019) 534–540.

[28] S. Li, Q. Meng, S. Lü, W. Sun, Study on optical temperature sensing properties of Tb^{3+}, Eu^{3+} co-doped $CaMoO_4$ phosphor, J. Lumin. 200 (2018) 103–110.

[29] Y. Ding, J. Liu, Y. Zhu, S. Nie, W. Wang, J. Shi, Y. Miu, X. Yu, Brightly luminescent and color-tunable $CaMoO_4$: RE^{3+}(RE= Eu, Sm, Dy, Tb) nanofibers synthesized through a facile route for efficient light-emitting diodes, J. Mater. Sci. 53 (2018) 4861–4873.

[30] G. Botelho, I.C. Nogueira, E. Moraes, E. Longo, Study of structural and optical properties of $CaMoO_4$ nanoparticles synthesized by the microwave-assisted solvothermal method, Mater. Chem. Phys. 183 (2016) 110–120.

[31] G.M. Gurgel, L.X. Lovisa, L.M. Pereira, F.V. Motta, M.S. Li, E. Longo, C. A. Paskocimas, M.R.D. Bomio, Photoluminescence properties of (Eu, Tb, Tm) co-doped $PbMoO_4$ obtained by sonochemical synthesis, J. Alloys Compd. 700 (2017) 130–137.

[32] J.H. Bang, K.S. Suslick, Applications of Ultrasound to the Synthesis of Nanostructured Materials, Advanced Materials 22 (2010) 1039–1059.

[33] F. Dong, L. Wu, Y. Sun, M. Fu, Z. Wu, S.C. Lee, Efficient synthesis of polymeric g-C_3N_4 layered materials as novel efficient visible light driven photocatalysts, J. Mater. Chem. 21 (2011) 15171–15174.

[34] H. Rietveld, A profile refinement method for nuclear and magnetic structures, J Appl Crystallogr 2 (1969) 65–71.

[35] B. Toby, EXPGUI, a graphical user interface for GSAS, J Appl Crystallogr 34 (2001) 210–213.

[36] L. Zhu, Y. Mao, Q. Chen, Y. Zou, X. Shen, G. Liao, Synthesis and optical properties of coil-ball-like $CaMoO_4$ hierarchical architectures, J. Mater. Sci. Mater. Electron. 30 (2019) 3639–3646.

[37] A.K.V. Raj, P. Prabhakar Rao, T.S. Sreena, T.R. Aju Thara, Broad greenish-yellow luminescence in $CaMoO_4$ by Si^{4+} acceptor doping as potential phosphors for white light emitting diode applications, J. Mater. Sci. Mater. Electron. 29 (2018) 16647–16653.

[38] V. Panchal, N. Garg, H.K. Poswal, D. Errandonea, P. Rodríguez-Hernández, A. Muñoz, E. Cavalli, High-pressure behavior of $CaMoO_4$, Phys. Rev. Mater. 1 (2017), 043605.

[39] R. Bhosale, S. Jain, C.P. Vinod, S. Kumar, S. Ogale, Direct Z-Scheme g-C_3N_4/$FeWO_4$ Nanocomposite for Enhanced and Selective Photocatalytic CO_2 Reduction under Visible Light, ACS Appl Mater Interfaces 11 (2019) 6174–6183.

[40] F.K.F. Oliveira, M.C. Oliveira, L. Gracia, R.L. Tranquilin, C.A. Paskocimas, F. V. Motta, E. Longo, J. Andrés, M.R.D. Bomio, Experimental and theoretical study to explain the morphology of $CaMoO_4$ crystals, J Phys Chem Solids 114 (2018) 141–152.

[41] K. Momma, F. Izumi, VESTA 3 for three-dimensional visualization of crystal, volumetric and morphology data, J Appl Crystallogr 44 (2011) 1272–1276.

[42] B.P. Singh, A.K. Parchur, R.S. Ningthoujam, A.A. Ansari, P. Singh, S.B. Rai, Influence of Gd^{3+} co-doping on structural property of $CaMoO_4$:Eu nanoparticles, Dalton Trans 43 (2014) 4770–4778.

[43] A.K. Parchur, R.S. Ningthoujam, Preparation and structure refinement of Eu^{3+} doped $CaMoO_4$ nanoparticles, Dalton Trans 40 (2011) 7590–7594.

[44] B. Zhu, P. Xia, Y. Li, W. Ho, J. Yu, Fabrication and photocatalytic activity enhanced mechanism of direct Z-scheme g-C_3N_4 /Ag_2WO_4 photocatalyst, Appl. Surf. Sci. 391 (2017) 175–183.

[45] X. Chen, D.-H. Kuo, D. Lu, Nanonization of g-C_3N_4 with the assistance of activated carbon for improved visible light photocatalysis, RSC Adv 6 (2016) 66814–66821.

[46] S. Dutta, S. Som, S.K. Sharma, Excitation spectra and luminescence decay analysis of K^+ compensated Dy^{3+} doped $CaMoO_4$ phosphors, RSC Adv 5 (2015) 7380–7387.

[47] R.L. Tranquilin, L.X. Lovisa, C.R.R. Almeida, C.A. Paskocimas, M.S. Li, M. C. Oliveira, L. Gracia, J. Andres, E. Longo, F.V. Motta, M.R.D. Bomio, Understanding the White-Emitting $CaMoO_4$ Co-Doped Eu^{3+}, Tb^{3+}, and Tm^{3+} Phosphor through Experiment and Computation, J. Phys. Chem. C 123 (2019) 18536–18550.

[48] A.A.G. Santiago, R.L. Tranquilin, P. Botella, F.J. Manjón, D. Errandonea, C. A. Paskocimas, F.V. Motta, M.R.D. Bomio, Spray pyrolysis synthesis and characterization of $Mg_{1-x}Sr_xMoO_4$ heterostructure with white light emission, J. Alloys Compd. 813 (2020), 152235.

[49] V.S. Marques, L.S. Cavalcante, J.C. Sczancoski, A.F.P. Alcântara, M.O. Orlandi, E. Moraes, E. Longo, J.A. Varela, M.Siu Li, M.R.M.C. Santos, Effect of Different Solvent Ratios (Water/Ethylene Glycol) on the Growth Process of $CaMoO_4$ Crystals and Their Optical Properties, Cryst. Growth Des. 10 (2010) 4752–4768.

[50] H. Zhao, Y. Dong, P. Jiang, H. Miao, G. Wang, J. Zhang, In situ light-assisted preparation of MoS_2 on graphitic C_3N_4 nanosheets for enhanced photocatalytic H_2 production from water, J. Mater. Chem. A 3 (2015) 7375–7381.

[51] Y. Shiraishi, S. Kanazawa, Y. Sugano, D. Tsukamoto, H. Sakamoto, S. Ichikawa, T. Hirai, Highly Selective Production of Hydrogen Peroxide on Graphitic Carbon Nitride (g-C_3N_4) Photocatalyst Activated by Visible Light, ACS Catal 4 (2014) 774–780.

[52] J. Zhang, L. Li, W. Zi, N. Guo, L. Zou, S. Gan, G. Ji, Self-assembled $CaMoO_4$ and $CaMoO_4$:Eu^{3+} hierarchical superstructures: Facile sonochemical route synthesis and tunable luminescent properties, J Phys Chem Solids 75 (2014) 878–887.

[53] Y. Wang, L. Yang, Y. Wang, X. Wang, G. Han, Controlled synthesis of $CaMoO_4$ and $SrMoO_4$ rods by a simple sonochemical method, J. Ceram. Soc. JAPAN 120 (2012) 378–381.

[54] Y. Tian, F. Cheng, X. Zhang, F. Yan, B. Zhou, Z. Chen, J. Liu, F. Xi, X. Dong, Solvothermal synthesis and enhanced visible light photocatalytic activity of novel graphitic carbon nitride–Bi_2MoO_6 heterojunctions, Powder Technol 267 (2014) 126–133.

[55] L. Tolvaj, K. Mitsui, D. Varga, Validity limits of Kubelka–Munk theory for DRIFT spectra of photodegraded solid wood, Wood Sci. Technol. 45 (2011) 135–146.

[56] D.L. Wood, J. Tauc, Weak Absorption Tails in Amorphous Semiconductors, Phys. Rev. B 5 (1972) 3144–3151.

[57] D. Errandonea, A. Muñoz, P. Rodríguez-Hernández, J.E. Proctor, F. Sapiña, M. Bettinelli, Theoretical and Experimental Study of the Crystal Structures, Lattice Vibrations, and Band Structures of Monazite-Type $PbCrO_4$, $PbSeO_4$, $SrCrO_4$, and $SrSeO_4$, Inorg. Chem. 54 (2015) 7524–7535.

[58] V. Monteseguro, J. Ruiz-Fuertes, J. Contreras-García, P. Rodríguez-Hernández, A. Muñoz, D. Errandonea, High pressure theoretical and experimental analysis of the bandgap of $BaMoO_4$, $PbMoO_4$, and $CdMoO_4$, Appl. Phys. Lett. 115 (2019), 012102.

[59] A.A.G. Santiago, C.R.R. Almeida, R.L. Tranquilin, R.M. Nascimento, C. A. Paskocimas, E. Longo, F.V. Motta, M.R.D. Bomio, Photoluminescent properties of the $Ba_{1-x}Zn_xMoO_4$ heterostructure obtained by ultrasonic spray pyrolysis, Ceram. Int. 44 (2018) 3775–3786.

[60] S. Dutta, S. Som, A.K. Kunti, V. Kumar, S.K. Sharma, H.C. Swart, H.G. Visser, Structural and luminescence responses of $CaMoO_4$ nano phosphors synthesized by hydrothermal route to swift heavy ion irradiation: Elemental and spectral stability, Acta Mater 124 (2017) 109–119.

[61] A. Pandey, V. Kumar, S. Som, A. Yousif, R.E. Kroon, E. Coetsee, H.C. Swart, Photon and electron beam pumped luminescence of Ho^{3+} activated $CaMoO_4$ phosphor, Appl. Surf. Sci. 423 (2017) 1169–1175.

[62] P. Praus, L. Svoboda, M. Ritz, I. Troppová, M. Šihor, K. Kočí, Graphitic carbon nitride: Synthesis, characterization and photocatalytic decomposition of nitrous oxide, Mater. Chem. Phys. 193 (2017) 438–446.

[63] L. Svoboda, P. Praus, M.J. Lima, M.J. Sampaio, D. Matýsek, M. Ritz, R. Dvorský, J. L. Faria, C.G. Silva, Graphitic carbon nitride nanosheets as highly efficient photocatalysts for phenol degradation under high-power visible LED irradiation, Mater. Res. Bull. 100 (2018) 322–332.

[64] W. Liu, J. Zhou, J. Yao, Shuttle-like CeO_2/g-C_3N_4 composite combined with persulfate for the enhanced photocatalytic degradation of norfloxacin under visible light, Ecotoxicol Environ Saf 190 (2020), 110062.

[65] W. Zhang, C. Xu, E. Liu, J. Fan, X. Hu, Facile strategy to construction Z-scheme $ZnCo_2O_4$/g-C_3N_4 photocatalyst with efficient H_2 evolution activity, Appl. Surf. Sci. 515 (2020), 146039.

[66] L. Wang, Q. Song, X. Guo, N. Wang, X. Wang, Y. Han, J. Xie, Synthesis of hollow spindle-like $CaMoO_4$: Ln^{3+}(Tb, Eu) phosphors for detection of iron(III) ions, Optik 185 (2019) 957–964.

[67] A.M. Huerta-Flores, I. Juárez-Ramírez, L.M. Torres-Martínez, J.E. Carrera-Crespo, T. Gómez-Bustamante, O. Sarabia-Ramos, Synthesis of $AMoO_4$ (A = Ca, Sr, Ba) photocatalysts and their potential application for hydrogen evolution and the degradation of tetracycline in water, J. Photochem. Photobiol. A 356 (2018) 29–37.

[68] Y.-S. Luo, X.-J. Dai, W.-D. Zhang, Y. Yang, C.Q. Sun, S.-Y. Fu, Controllable synthesis and luminescent properties of novel erythrocyte-like $CaMoO_4$ hierarchical nanostructures via a simple surfactant-free hydrothermal route, Dalton Trans 39 (2010) 2226–2231.

[69] M.M. Momeni, M. Hakimian, A. Kazempour, In-situ manganese doping of TiO_2 nanostructures via single-step electrochemical anodizing of titanium in an electrolyte containing potassium permanganate: A good visible-light photocatalyst, Ceram. Int. 41 (2015) 13692–13701.

[70] S.R. Morrison, Electrochemistry at semiconductor and oxidized metal electrodes, (1980).

[71] M. Mousavi, A. Habibi-Yangjeh, M. Abitorabi, Fabrication of novel magnetically separable nanocomposites using graphitic carbon nitride, silver phosphate and silver chloride and their applications in photocatalytic removal of different pollutants using visible-light irradiation, J. Colloid Interface Sci. 480 (2016) 218–231.

[72] K. Dai, L. Lu, C. Liang, G. Zhu, Q. Liu, L. Geng, J. He, A high efficient graphitic-C_3N_4/BiOI/graphene oxide ternary nanocomposite heterostructured photocatalyst with graphene oxide as electron transport buffer material, Dalton Trans 44 (2015) 7903–7910.

[73] S. Deng, W. Zhang, Z. Hu, Z. Feng, P. Hu, H. Wu, L. Ma, Y. Pan, Y. Zhu, G. Xiong, Dual-functional Bi^{3+}, Dy^{3+} co-doping $ZnWO_4$ for photoluminescence and photocatalysis, Appl. Phys. A 124 (2018) 526.